Experimental Observations of a Spherical Transparent Cathode Glow Discharge

Ryan M. Meyer, *Member, IEEE*, Mark A. Prelas, *Member, IEEE*, and Sudarshan K. Loyalka

Abstract—In this paper, several observations with regard to the nature of the glow discharge in a spherical inertial electrostatic-confinement device are reported. In particular, automated single and double Langmuir probe diagnostics are configured such that the ion-microchanneling phenomenon is directly verified. In addition, these measurements allow for the determination of the "star-to-jet" mode transition and show that microchanneling persists well into jet-mode regime despite its visual appearance. Conclusions about the overall discharge structure may also be drawn from spatial variations in the density and neutrality of the discharge. Finally, I–V characteristics obtained with the double Langmuir probe indicate the presence of energetic electrons inside of the cathode-grid region.

Index Terms—Electrostatic devices, glow discharge, inertial confinement, neutron generator.

I. INTRODUCTION

THE STUDY of a unique glow discharge (GD) of spherical geometry with a fully enclosed partially transparent cathode is motivated by continued investigations of inertial electrostatic confinement (IEC). IEC is a means to confine ions for fusion purposes with electrostatic fields, developed almost simultaneously by Farnsworth [1], [2] and Lavrent'ev [3] in the 1950s and 1960s. GD IEC is of particular interest for its engineering simplicity and potential for immediate entry into neutron-source markets [4]. Development of the GD mode of operation was instigated by Miley *et al.* [4]–[16] at the University of Illinois at Urbana–Champaign (UIUC) in the early 1990s, evolving from the seminal works of Farnsworth [1], [2], Lavrent'ev [3], and Hirsch [17].

In the GD IEC, both the anode and cathode are enclosed in a vacuum chamber to operate at pressures of approximately 0.1–7.0 Pa (1–50 mtorr). A large electric-potential difference is applied to the two electrodes, ionizing the working gas. Resulting ions are accelerated by the relative negative potential of the cathode and oscillate through the transparent electrode a number of times before removal from the system. The oscillating nature of the ions amplifies the probability that the trajectories of two isolated ions will intersect near the center of the device and perhaps undergo fusion. However, GD mode of operation occurs at such pressures that interactions between energetic particles and the neutral background gas dominate the fusion reactivity, and the number of oscillations is approximately one.

Two submodes have been noted within the GD mode of IEC operation. These modes are star and jet modes, respectively [5]. Generally, star mode may be observed over the pressure range of ∼0.1–3.0 Pa (1–25 mtorr), while jet mode occurs at greater pressures: ∼3.0–7.0 Pa (25–50 mtorr). Visually, star mode is distinguished by spokes of light emanating through most of the grid holes. These spokes of light are known as "ion microchannels." Ion-microchannel formation has been the focus of considerable theoretical and computational studies at UIUC [7], [11]–[16]. Since thorough discussions of ion microchanneling exist in the literature, we only note that the microchanneling phenomenon is a result of the curvature in equipotential surfaces near the cathode grid, due to its discrete nature. Thus, microchanneling is a function of the plasma state, cathode potential, and grid hole size. Jet mode has received less attention because its operational regime occurs at cathode voltages insufficient to cause appreciable fusion reactions. Jet mode is visually more uniform than star mode, with the exception of a single "electron-jet" protruding through one of the cathode-grid holes.

Much of what is known about star-mode microchanneling is the outcome of theory and simulation [7], [11]–[13], [15], [16]. Maximizing total neutron output has been the goal of many experimental investigations; however, it does not appear that any attempt has been made to directly verify microchannel theory [5], [6], [9]–[11], [13], [14], [18]. We have explored in this paper the structures of star- and jet-mode discharges experimentally with automated single and double Langmuir probe diagnostics in a spherical IEC (SIEC) device. The experimental setup, discussed in Section II, is configured such that microchanneling phenomenon can be evaluated. This evaluation is based on I–V characteristics and the resulting measurements of the ion and electron densities, presented in Section III. In Section IV, the implication of our results is discussed with respect to the overall discharge structure and neutrality, the star-to-jet mode transition, the electron species, verification of the microchanneling phenomenon, as well as the observation that microchanneling persists well into the jet-mode regime.

II. EXPERIMENTAL SETUP

This section provides a description of the physical GD SIEC apparatus in the Nuclear Science and Engineering Institute at the University of Missouri-Columbia (UMC). Descriptions
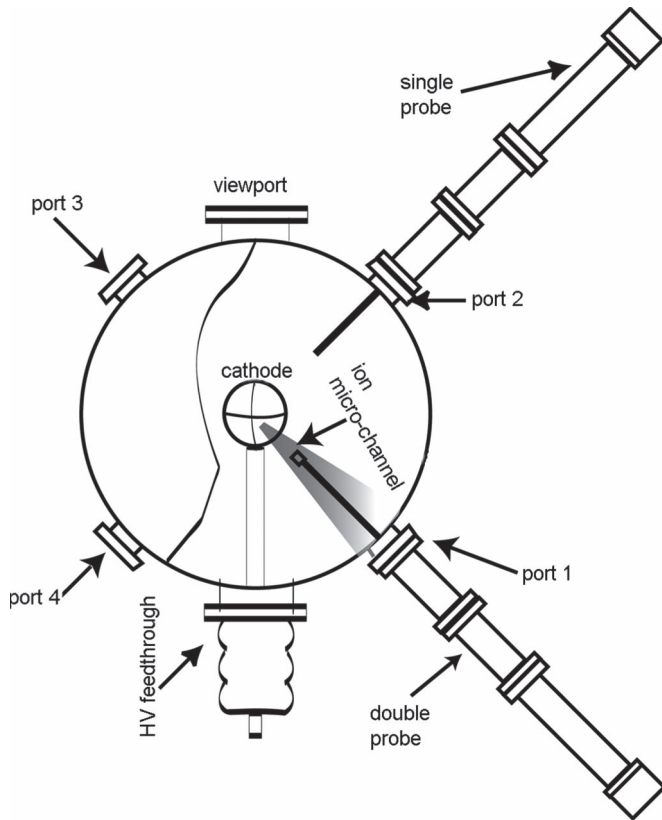
Fig. 1. Top view of the GD SIEC at UMC. Four 7-cm (2–3/4 in) conflat flanges are indicated for electrostatic-probe access. These access ports are labeled as "port 1–4" in the diagram. Also indicated are the HV feedthrough, the viewport, the double Langmuir probes, the single Langmuir probe, the cathode, and an ion microchannel. The ion microchannel is depicted to emphasize the observed phenomena of microchannel formation in the direction of port 1 and the absence of an accessible microchannel to a probe inserted at port 2.

of the electrostatic-probe diagnostics are included, also, as equipment is described in the following sequence: 1) vacuum chamber and system, 2) electrodes, and 3) electrostatic-probe diagnostics. A brief discussion of the technique used to analyze single and double Langmuir probe $I–V$ characteristics follows the description of equipment.

A. Vacuum Chamber and System

Spherical electrodes are enclosed within a cylindrical stainless-steel bell jar that has an 46-cm inner diameter and is 76 cm tall. The bell jar consists of four 7-cm (2–3/4 in) conflat flanges at 30 cm from the bottom of the jar for electrostatic-probe access and two opposing 15-cm viewports, also at 30 cm from the bottom of the bell jar, as shown in Fig. 1. One of the viewports is used as an access port for the cathode. The access ports for electrostatic probes are labeled as "ports 1–4" in Fig. 1. An ion microchannel is also depicted, showing that an ion microchannel is consistently accessible to probes inserted into port 1, and no ion microchannel is accessible to probes inserted into port 2. Base pressures of 10^{-4} Pa (10^{-6} torr) are achieved with a turbomolecular pump that has a pumping capacity of 200 L/s before the chamber is back-filled with hydrogen gas to pressures in the range of 0.1–7.0 Pa (1–50 mtorr).

B. Electrodes

The anode grid, or "globe," is formed via 46-cm-diameter rings of 6.35-mm-diameter stainless-steel tubing. It consists of three rings forming six lines of longitude, each separated by 60°. Five stainless-steel rings of latitude complete the structure, with access for electrostatic probes and the cathode feed through at the "equator." The anode is filled-in further by welding stainless-steel flat ribbon between the lines of longitude formed by the tubing.

The cathode grid is much smaller, having a diameter of 9.5 cm. It is typically constructed from stainless wire with a thickness of 1 mm. The cathode grid is formed by creating seven 9.5-cm-diameter rings, which are spot-welded together to form a "geodesic" pattern [13]. The geometric transparency of the cathode is, thus, $\eta \sim 0.94$. The cathode feedthrough is constructed out of a commercially available HV feedthrough, adapted to fit on one of the 15-cm viewports of the vacuum chamber, as shown in Fig. 1.

C. Langmuir Probe Implementations

The shaft of the double Langmuir probe is constructed from insulating alumina tubing with a 6.35-mm OD. An alumina silicate cup, with a base diameter of 13 mm and a length of 15 mm, is glued to the end of the probe shaft using an alumina adhesive. Circular depressions are drilled in one end of the cup for the placement of 3-mm-diameter molybdenum disks. In an attempt to decrease the size of the probe, much of the alumina silicate cup was ground off using a Dremel tool. Alumina tubing is also used for the shaft of a single Langmuir probe. In this case, a length of 3-mm-OD alumina tubing is adhered to the inner wall of a length of 6.35-mm-OD tubing in a telescope-like fashion. A 3-mm molybdenum disk is then glued to the end of the probe shaft.

The data-collection process is automated, as the $I–V$ characteristics are obtained at positional increments of 1 mm along the radius of the device. Probe motion is controlled with a motorized linear manipulator with a 100-mm stroke length. A NEMA 21 size stepper motor with a 0.9° step resolution is controlled with a unipolar stepper-motor driver, which receives the appropriate signals through LabVIEW. An optical encoder with 1000 counts per revolution resolution allows precise measurements of the probe position to within ~1 μm.

A triangular voltage sweep signal with an amplitude of 2000 V_{p-p} and a frequency of 0.5 Hz is generated with a function generator and bipolar operational amplifier (BOP), as shown in Fig. 2. For single-probe measurements, this sweep signal must be superimposed on the signal from a programmable high-voltage power supply, accomplished by closing switch, s1, in Fig. 2. The output of the programmable supply is specified after first collecting floating-potential data along the device radius.

D. Langmuir Probe Analysis

The methods employed for analyzing the $I–V$ curves from the double and single probes are discussed here. Planar-disk collectors are used in the experiments, and the method of analysis is based on a thin collisionless sheath assumption [19],
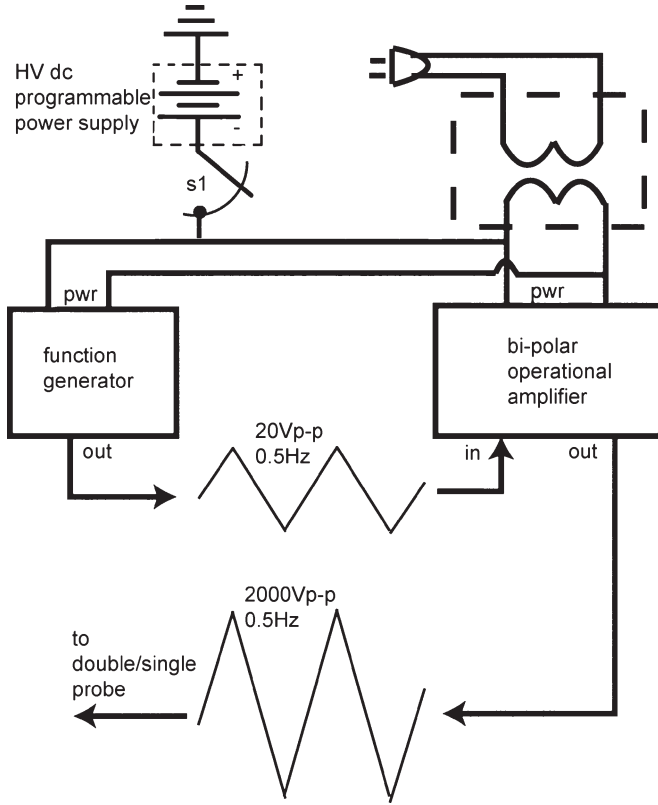
Fig. 2. Depiction of the voltage-sweeping scheme for the double Langmuir probe diagnostic. In this case, a 20-V_{p-p} triangular signal from the function generator is amplified to 2000 V_{p-p} by the BOP. For single-probe sweeping, the switch, s1, is closed to bias the probe with an HV dc power supply.

such that $x_s \ll \lambda$ and $x_s \ll a$, where λ represents the mean free path of ions or electrons, x_s is the sheath thickness, and a is the diameter of the planar collecting disk. In this case, the collected current is assumed to be equal to the amount of current which flows through the sheath boundary adjacent to the planar probe surface. Under this scenario, the kinetically derived currents to a negatively biased collector are

$$I_0 = 0.61 e n_\infty \left(\frac{kT_1}{m_0}\right)^{1/2} A \tag{1}$$

$$I_1 = -\frac{1}{4} e n_\infty \left(\frac{8kT_1}{\pi m_1}\right)^{1/2} e^{-e(V_\infty - V_p)/kT_1} A \tag{2}$$

where quantities with subscript zero are associated with ions and quantities with subscript one are associated with electrons. I_j, kT_j, and m_j are representative of the current, temperature, and mass, respectively, of a particular species j while n_∞ and V_∞ denote the plasma density and plasma potential, respectively. Finally, we note that e represents the magnitude of the electronic charge, V_p is the bias potential of the collecting disk, and A is the collecting area (here, assumed to be equal to the surface area of the collecting disk). The expression $(kT_1/m_0)^{1/2}$ in (1) is known as the Bohm velocity [19].

Analysis of single-probe I–V characteristics proceeds by subtracting I_0 from the total current I to the collecting disk, to obtain I_1. kT_1 can thus be obtained from

$$\frac{\partial \log(I_1)}{\partial V_p} = \frac{e}{kT_1}. \tag{3}$$

n_∞ is computed from the electron saturation current I_{1s}, obtained by setting $V_p = V_\infty$ in (2), thus

$$n_\infty = \frac{4I_{1s}}{e \left(\frac{8kT_1}{\pi m_1}\right)^{1/2} A}. \tag{4}$$

For the double-probe analysis, the two collecting disks are labeled as "a" and "b." The double probe withdraws no net charge from the plasma, satisfying the following condition:

$$I = I_{0a} + I_{1a} = -(I_{0b} + I_{1b}) \tag{5}$$

where I is the measured quantity or current flowing from one collector to the other through the sweeping circuit. Equation (5) can be manipulated, along with (2), so that the following expression is obtained:

$$I = I_0 \tan\left(\frac{e(V_a - V_b)}{2kT_1}\right). \tag{6}$$

It immediately follows that

$$\left.\frac{dI}{d(V_a - V_b)}\right|_{V_a = V_b} = \frac{eI_0}{2kT_1} \tag{7}$$

where I_0 is the ion saturation current, expressed by (1). Equation (1) can then be manipulated to yield n_∞ once a value for kT_1 is obtained [20].

III. EXPERIMENTAL RESULTS

Discharge-density data are obtained from single and double electrostatic-probe diagnostics, as discussed in Section II. Fig. 1 shows the experimental configuration with the single probe mounted at port 2 and the double probe mounted at port 1. Note that single-probe I–V characteristics are obtained with both the single and double probes (in the double-probe case, the sweep signal is only applied to one of the collecting disks of the double probe). In this section, we first present several individual single- and double-probe I–V characteristics obtained at ports 1 and 2 (these characteristics are germane to the discussions in Section IV regarding the electron populations and heterogeneous nature of the discharge). We then use these characteristics to deduce results for ion- and electron-density profiles for a range of experimental conditions. Tables I and II summarize the experimental conditions, and the respective data/results are shown in Figs. 3–6, 8 (Table I) and Fig. 7 (Table II).

A. I–V Characteristics

Generally, I–V traces obtained with the double Langmuir probe are not symmetrical. Several double-probe traces are shown in Fig. 3 and show that the current becomes zero at a nonzero voltage. This asymmetry is due to the strong electric fields inherent to IEC devices, and, as noted in a recent publication [22], the point of intersection of an I–V trace with the voltage axis is a measure of the tangential component of the electric field. In addition to the earlier asymmetry, several of the I–V characteristics exhibit another distinguishing feature,

TABLE I
SUMMARY OF DISCHARGE CONDITIONS FOR EXPERIMENTAL
DATA SHOWN IN FIGS. 3–6, AND 8

port	Figs.	P (mA kV$^{-3/2}$)	Vs (kV)	Is (mA)	discharge mode
1	3,6,8	4.22	-4.38	38.73	jet
1	6,8	3.42	-4.83	36.37	star
1	8	0.32	-4.96	3.50	star
1	8	6.00	-3.54	39.97	jet
1	4	0.93	-5.04	10.50	star
1	6	2.97	-4.98	33.07	star
1	6	1.19	-4.97	13.22	star
2	5(a)	2.49	-5.01	27.91	star
2	5(b)	5.48	-3.76	39.97	jet
2	5(c)	9.75	-2.56	39.97	jet

TABLE II
SUMMARY OF DISCHARGE CONDITIONS FOR
EXPERIMENTAL DATA SHOWN IN FIG. 7

	P (mA kV$^{-3/2}$)	Vs (kV)	Is (mA)	discharge mode
●	0.32	-5.03	3.58	star
■	0.37	-5.03	4.19	star
▲	0.93	-5.04	10.50	star
▼	1.02	-5.04	11.52	star
◆	3.93	-4.70	39.97	star
■	3.96	-4.67	39.97	star
●	5.20	-3.98	39.97	jet
♣	7.41	-3.08	39.97	jet
⬟	9.96	-2.53	39.97	jet

which manifests itself as a "bump" in the I–V characteristic for some negative values of voltage, as shown in Fig. 3. The cause of this feature is left for discussion in Section IV; however, here, we mention that such a feature consistently appears in the region $34 \text{ mm} \leq r \leq 42 \text{ mm}$, where the cathode-grid radius is $R_g = 47 \text{ mm}$ for reference.

Several single-probe traces along the radius of the device at port 1 are shown in Fig. 4 for a particular discharge condition. These I–V curves experience severe distortion, as the probe is inserted inside of the cathode and approaches the center. The distortion occurs because the single probe withdraws too many electrons from the plasma. The disturbance is so severe, in fact, that it produces a visually evident signal on the analog ammeter of the discharge power supply. Finally, several single-probe I–V characteristics, obtained at port 2, are shown in Fig. 5. The discharge is highly nonneutral in this location, as the floating potential is greater than or equal to the plasma potential.

B. Density Measurements

Ion-density profiles and some electron-density measurements for $r > R_g$ are obtained for several discharge conditions by analyzing I–V characteristics as discussed in Section II-D. The ion-density profiles are obtained from the double Langmuir probe sweeps at port 1 while electron-density measurements are obtained from single Langmuir probe sweeps at port 1. The ion-density profiles are shown in Fig. 6 while some electron-density measurements are shown in Fig. 7.

IV. DISCUSSIONS/CONCLUSION

We describe in this section several observations with respect to the overall discharge structure, the electron species, and several microchanneling properties based on the experimental results presented in Section III. The overall discharge structure is examined mostly in terms of neutrality and spatial variations in the densities. To study microchannel properties, we have to define what constitutes microchanneling. Since star mode is characterized by a number of "spokes" of light emanating through most (but not necessarily all) of the grid holes, we may detect microchanneling as a significant enhancement in electron or ion density for a grid hole with a spoke; compared to a grid hole with no spoke.

A. Discharge Structure, Ion Microchannel Characteristics

The excessive draining of electrons when the single Langmuir probe is located near the center of the device is certainly undesirable from a diagnostic viewpoint, but it is evidence that the electron density is significantly larger in this region. In addition, although I–V characteristics are distorted near the center, it is still possible to see from the curves that the electron temperature is very low, $\sim$10 eV, at this location. This is not surprising if we consider radial floating-potential profiles, as shown in Fig. 8. The profiles indicate a flat potential profile at the center of the device for nearly all cases under consideration.

Fig. 9 shows a plot obtained by averaging all ion-density measurements outside of the cathode grid (i.e., $r > R_g$) obtained with the double Langmuir probe at port 1. This is done for all discharge conditions so that a plot of the average densities with respect to P is obtained. A similar procedure can be followed for data collected from single Langmuir probe sweeps at ports 1 and 2. The results are all included together in Fig. 9. It is obvious from this plot that an ion microchannel is neutral over a very narrow range of P near $P = 4 \text{ mA} \cdot \text{kV}^{-3/2}$; at least for the experimental device under consideration. We note from Fig. 5 that, along a path where microchanneling is absent, the discharge is highly nonneutral and remains that way for all discharge conditions under consideration. Fig. 9 contains additional information, such as the star-to-jet mode transition, which also occurs near $P = 4 \text{ mA} \cdot \text{kV}^{-3/2}$. It appears that one feature distinguishing star and jet modes is the scaling of ion and electron densities with P along an ion microchannel. Finally, microchanneling phenomenon is identified by differences in measured electron densities at ports 1 and 2. Fig. 9 shows that microchanneling persists well into the jet-mode regime despite its visual appearance.

B. Electron Populations

As discussed in the last section, the plots shown Fig. 3 exhibit an interesting feature. This feature is the result of secondary electron emission from the molybdenum collecting disks of the double probe, indicating the presence of high-energy
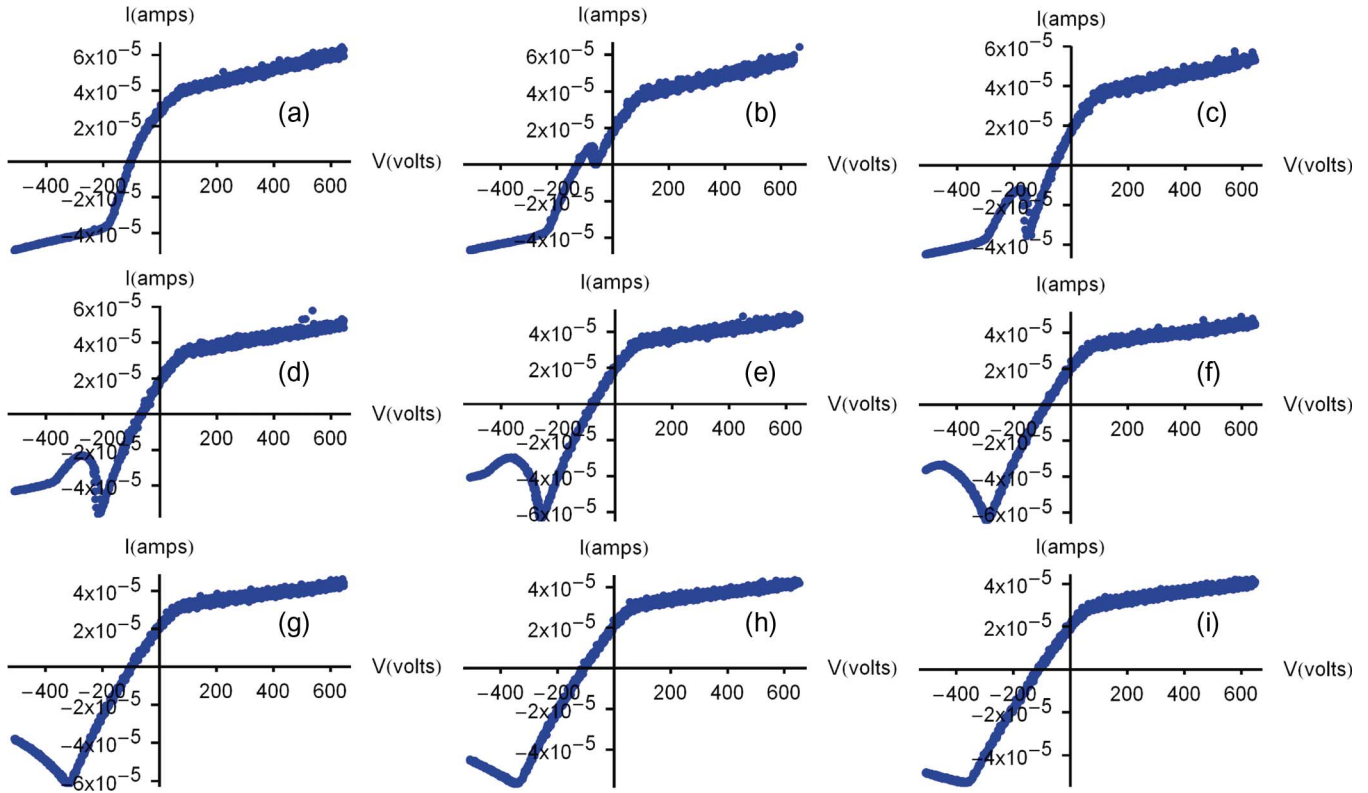
Fig. 3. Several double Langmuir probe I–V characteristics obtained from port 1 for the discharge conditions $Vs = -4.38$ kV, $Is = 38.73$ mA, and $P = 4.22$ mA $\cdot$ kV$^{-3/2}$. The I–V characteristics are obtained at (a)–(i) $r = 33, 34, 35, 36, 37, 38, 39, 40,$ and 41 mm. The cathode grid is located at $r = 47$ mm.
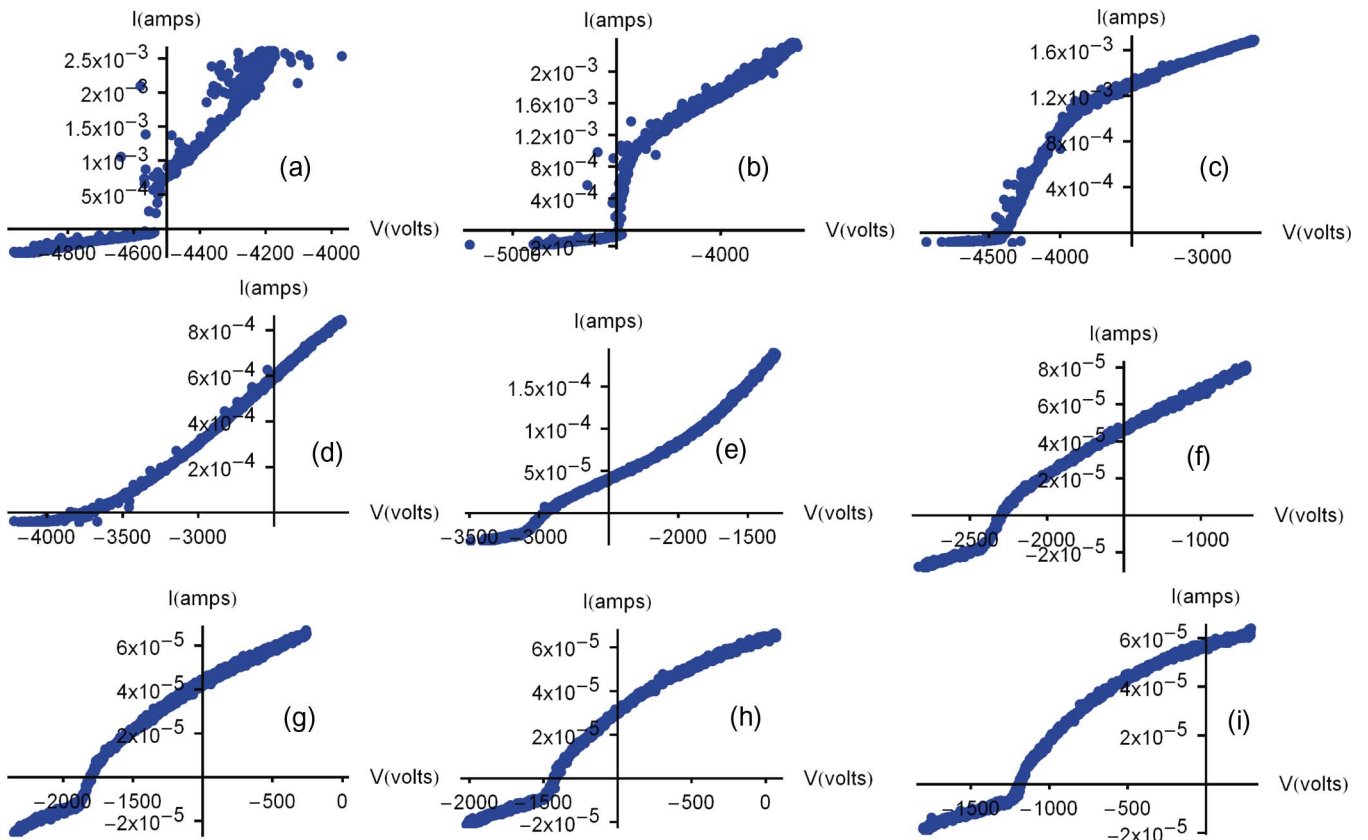

Fig. 4. Several single Langmuir probe I–V characteristics obtained from port 1. The I–V characteristics are obtained at (a)–(i) $r = 10, 20, 30, 40, 50, 60, 70, 80$ and 90 mm. The cathode grid is located at $r = 47$ mm.
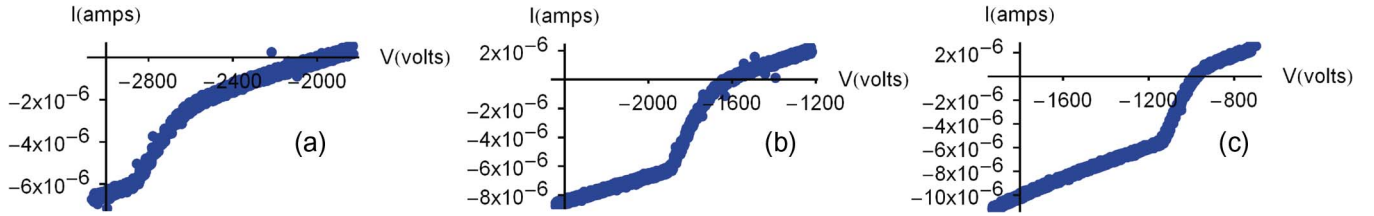
Fig. 5. Single Langmuir probe I–V characteristics obtained at port 2 for (a) $P = 2.49$ mA $\cdot$ kV$^{-3/2}$, (b) $P = 5.48$ mA $\cdot$ kV$^{-3/2}$, and (c) $P = 9.75$ mA $\cdot$ kV$^{-3/2}$.
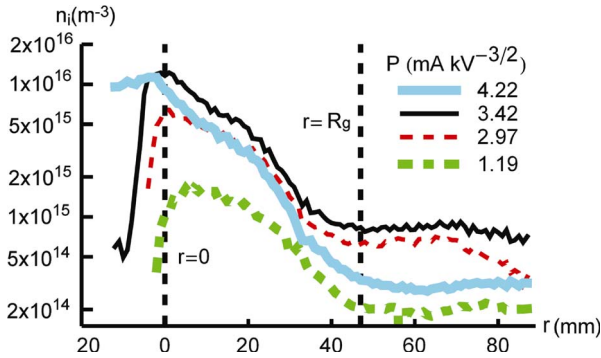

Fig. 6. Radial profiles of the ion density $n_i(r)$ for several discharge conditions as specified in Table I.
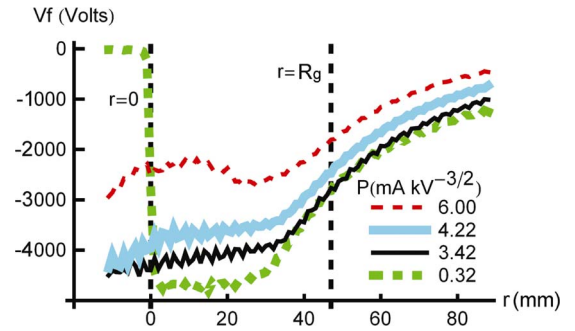

Fig. 8. Radial floating-potential profiles for several discharge conditions as specified in Table I.
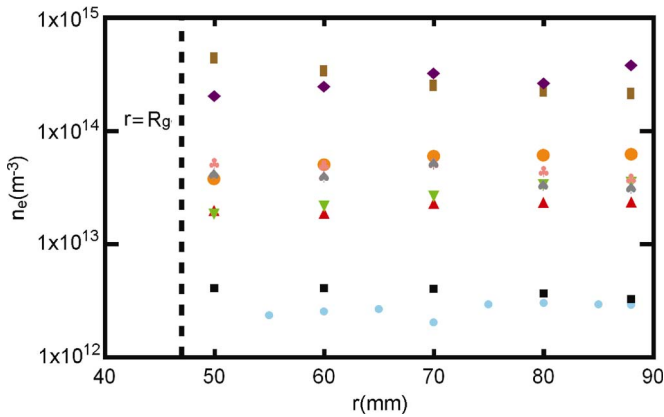

Fig. 7. Several electron-density measurements obtained at port 1 (i.e., along an ion microchannel) for $r > R_g$ and several discharge conditions listed in Table II.
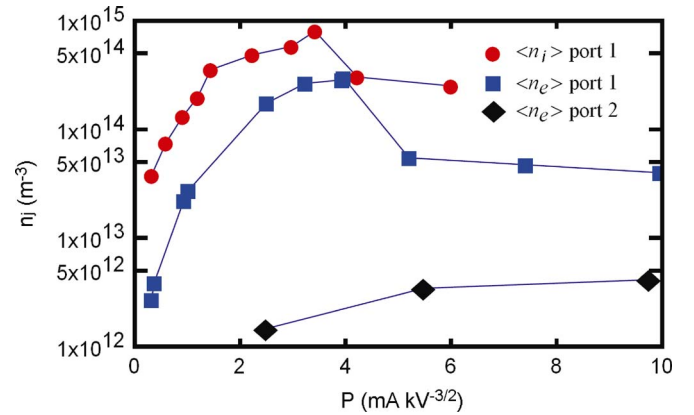

Fig. 9. Ion- and electron-density measurements for $r > R_g$ are averaged for each discharge condition and plotted versus P.

electrons [23]. The same phenomenon is observed with single Langmuir sweeps, as shown in Fig. 10, but is much less obvious. This population of high-energy electrons is similar to the well-known primary electrons of conventional parallel-plate GDs [21]; however, in this case, the electrons do not originate from the cathode. This is obvious because the electrons are detected well within the cathode grid. Instead, if we observe the radial floating-potential profiles shown in Fig. 8, we note that the profiles show flattening for $r \leq 34$ mm. This location is coincident with the radial position at which the feature observed in the characteristics of Fig. 3 begins to appear. Thus, the source of this high-energy electron species is the distribution of low-temperature (~ 10 eV) electrons near the center of the device. Some of these electrons drift away from the center until they reach $r \sim 34$ mm and are then accelerated out of the cathode

by the electric field. From Fig. 3, it is evident that the energy, as well as the energy spread of these electrons, increases with increasing r.

C. Summary/Limitations

A single and double Langmuir probe are automated, and characteristics are thus obtained in fine positional increments (every 1 mm) over a portion of the device that includes the inner cathode region and a portion of the interelectrode space nearest the cathode. The curves are analyzed to characterize the discharge structure, microchanneling phenomena, and the electron species. Some of the most notable observations include the following: neutralization of a microchannel near $P \sim 4$ mA $\cdot$ kV$^{-3/2}$, transition from star mode to jet mode near $P \sim 4$ mA $\cdot$ kV$^{-3/2}$, persistence of microchanneling well into
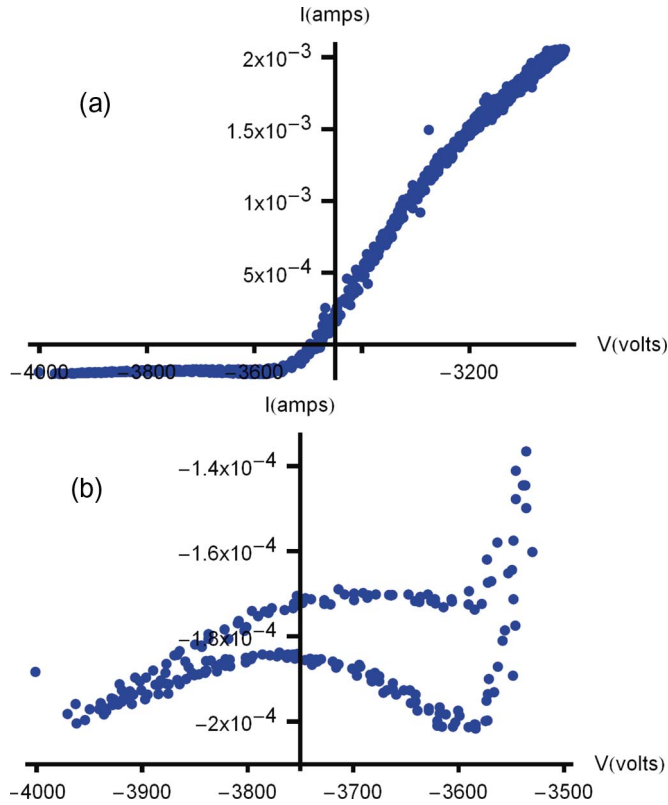
Fig. 10. (a) Single Langmuir probe I–V characteristic obtained at $r = 37$ mm. (b) Magnified view of the left side of the curve in (a) reveals a "bump," similar to what is observed with the double probe shown in Fig. 3. The splitting of the curve in (b) is due to the leakage capacitance of the sweeping circuit.

the jet-mode regime, and the existence of a population of high-energy electrons within the cathode-grid region.

We note that several assumptions were made in the analysis of the probe characteristics. Plasma conditions within a GD IEC are very diverse (indeed, that is one of the principle observations reported here), varying with space and pressure. To provide an illustration of when the assumptions are on the border of reality (or beyond), we have tabulated the relationship between several fundamental parameters for various spatial locations within GD IEC, and for several discharge conditions, in Table III. Utilizing the classification scheme of Demidov *et al.* [24], we wish to determine the relationship between the mean free paths of charged particles λ_j, the sheath thickness x_s, the probe dimension $a(= 3$ mm$)$, and the energy relaxation lengths of charged particles $\lambda_{\varepsilon j}$, where $j = 0$ identifies properties of ions and $j = 1$ identifies properties of electrons, consistent with Section II-D. We assume that $x_s \approx \lambda_D$ (the Debye length), where

$$\lambda_D = \sqrt{\frac{\varepsilon k T_1}{n_1 e^2}}. \tag{8}$$

In addition, the ionization fraction within GD SIEC is $< 0.1\%$, so we consider only interactions of charged particles with neutral molecules. Furthermore, we assume that $\lambda_1 = \lambda_0 = \lambda$ and consider only elastic collisions. For our purposes, we assume that the elastic-collision cross section σ_e is independent

of energy and has a value of 3×10^{-19} m^2. The mean free path is related to σ_e by

$$\lambda = \frac{1}{n\sigma_e} \tag{9}$$

where n is the neutral density related to pressure (in torr) p, with

$$n = 3.22 \times 10^{22} p. \tag{10}$$

In Table III, a pressure of 1 mtorr is assumed for discharge conditions $P \sim 0.30$ and 1.00 mA $\cdot$ kV$^{-3/2}$, while a pressure of 25 mtorr is assumed for $P \sim 4.00$ mA $\cdot$ kV$^{-3/2}$. Finally, we mention that $\lambda_{\varepsilon 0} = \lambda$ and $\lambda_{\varepsilon 1} \sim 45\lambda$, where $(45)^2$ is the estimated number of collisions required for an electron to lose its energy through elastic collisions with neutral hydrogen molecules.

In Table III, the SIEC is spatially separated into regions with respect to radius. The region $r < R_c$ $(R_c \sim 34$ mm$)$ is defined as a single region. The region $r > R_c$ is further subdivided with respect to microchannel regions and "microchannel-absent" regions. These subregions are denoted in Table III as "port 1" and "port 2," following the convention of Fig. 1. The electron densities reported in Table III are obtained from Fig. 6, for $r < R_c$, where it is assumed that $n_1 \approx n_0$, and from Fig. 9, for $r > R_c$. Values of λ_D are computed for $kT_1 = 10$ and 100 eV, representing the lower and upper bounds of kT_1 for the region $r > R_c$. For $r < R_c$, λ_D is computed assuming $kT_1 = 10$ eV. Here, R_c defines the region at the center of the device where $n_0 \approx n_1$, and the electric field is negligible. It should not be confused with the concept of "core radius" discussed in [22]. Table III reveals that the theory, discussed in Section II-D, relating plasma parameters to the probe signals is mostly valid for $r < R_c$. For $r > R_c$, however, transitional regimes are more dominant.

A further limitation of the theory presented in Section II-D is the naïve assumption that the electron distribution function is isotropic. GD IECs consist of weakly ionized plasma and, for a significant portion of its operational regime, can be characterized as weakly collisional. This, coupled with the presence of strong electric fields, creates an environment in which electrons gain more energy from the electric field than they lose through collisions. As a result, the distribution function of the electrons may become anisotropic, and the anisotropy may manifest itself as a Druyvesteyn distribution and/or beam components.

Given that electric fields are absent, or negligible, for $r < R_c$, the distribution function is likely to remain isotropic in this region. Beam components are most likely to appear near the cathode grid where the electric fields are strongest, and, indeed, this is one of the significant observations reported here. Work on more conventional GDs has already revealed that plasma waves can cause primary electron beams to lose their energy much faster than they would be expected to, based on collisions with neutral molecules alone. We consider that to be a likely scenario here, also, as all beam observations were made in a relatively small region inside of the cathode grid, and beams were not observed between the cathode and anode grids, even for discharge conditions with relatively large mean free paths,

TABLE III
PLASMA REGIMES WITHIN THE GD SIEC CLASSIFIED (FOLLOWING THE ORGANIZATIONAL SCHEME OF DEMIDOV *et al.* [24]) WITH RESPECT TO PARAMETERS λ, $\lambda_{\varepsilon 1}$, $\lambda_{\varepsilon 0}$, a, AND λ_D, REPRESENTING THE MEAN FREE PATH FOR IONS AND ELECTRONS, THE ENERGY RELAXATION LENGTH OF ELECTRONS, THE ENERGY RELAXATION LENGTH OF IONS, THE PROBE DIMENSION, AND THE DEBYE LENGTH, RESPECTIVELY, FOR SEVERAL EXPERIMENTAL CONDITIONS DISCUSSED IN SECTION II

	P (mA kV$^{-3/2}$)	n (m^{-3})	$\lambda \& \lambda_{\varepsilon 0}$ (m)	$\lambda_{\varepsilon 1}$ (m)		n_1 (m^{-3})	kT_1 (eV)	λ_D (m)	Parameter Relation, Regimes
$r<R_c$	~1.0	3.2×10^{19}	1×10^{-1}	0.45×10^{1}		1×10^{15}	10	7.4×10^{-4}	$\lambda_{\varepsilon 1} \gg \lambda \& \lambda_{\varepsilon 0} \gg a \gg \lambda_D$ collisionless, thin sheath
	~4.0	8.0×10^{20}	4×10^{-3}	1.8×10^{-1}		5×10^{15}	10	3.3×10^{-4}	$\lambda_{\varepsilon 1} \gg \lambda \& \lambda_{\varepsilon 0} \approx a \gg \lambda_D$ collisionless, thin sheath
$r>R_c$	~0.3	3.2×10^{19}	1×10^{-1}	0.45×10^{1}	port 1	2×10^{12}	10	1.7×10^{-2}	$\lambda_{\varepsilon 1} \gg \lambda \& \lambda_{\varepsilon 0} \gg \lambda_D \gg a$ collisionless, thick sheath
							100	5.3×10^{-2}	$\lambda_{\varepsilon 1} \gg \lambda \& \lambda_{\varepsilon 0} \approx \lambda_D \gg a$ collisionless - nonlocal transition, thick sheath
					port 2	1×10^{12}	10	2.4×10^{-2}	$\lambda_{\varepsilon 1} \gg \lambda \& \lambda_{\varepsilon 0} \gg \lambda_D \gg a$ collisionless, thick sheath
							100	7.4×10^{-2}	$\lambda_{\varepsilon 1} \gg \lambda \& \lambda_{\varepsilon 0} \approx \lambda_D \gg a$ collisionless - nonlocal transition, thick sheath
	~1.0	3.2×10^{19}	1×10^{-1}	0.45×10^{1}	port 1	2×10^{13}	10	5.3×10^{-3}	$\lambda_{\varepsilon 1} \gg \lambda \& \lambda_{\varepsilon 0} \gg \lambda_D \approx a$ collisionless, thin - thick sheath transition
							100	1.7×10^{-2}	$\lambda_{\varepsilon 1} \gg \lambda \& \lambda_{\varepsilon 0} \gg \lambda_D \gg a$ collisionless, thick sheath
					port 2	1×10^{12}	10	2.4×10^{-2}	$\lambda_{\varepsilon 1} \gg \lambda \& \lambda_{\varepsilon 0} \gg \lambda_D \gg a$ collisionless, thick sheath
							100	7.4×10^{-2}	$\lambda_{\varepsilon 1} \gg \lambda \& \lambda_{\varepsilon 0} \approx \lambda_D \gg a$ collisionless - nonlocal transition, thick sheath
	~4.0	8.0×10^{20}	4×10^{-3}	1.8×10^{-1}	port 1	2×10^{14}	10	1.7×10^{-3}	$\lambda_{\varepsilon 1} \gg \lambda_D \approx \lambda \& \lambda_{\varepsilon 0} \approx a$ collisionless - nonlocal transition, thin - thick sheath transition
							100	5.3×10^{-3}	$\lambda_{\varepsilon 1} \gg \lambda_D \approx \lambda \& \lambda_{\varepsilon 0} \approx a$ collisionless - nonlocal transition, thin - thick sheath transition
					port 2	5×10^{12}	10	1.1×10^{-2}	$\lambda_{\varepsilon 1} \gg \lambda_D \approx \lambda \& \lambda_{\varepsilon 0} \approx a$ collisionless - nonlocal transition, thin - thick sheath transition
							100	3.3×10^{-2}	$\lambda_{\varepsilon 1} \gg \lambda_D \gg a \approx \lambda \& \lambda_{\varepsilon 0}$ nonlocal, thick sheath

$\lambda \sim 10$ cm (in this case, an electron would be expected to undergo two to three collisions before reaching the anode). Thus, we conclude that beams are present but suspect that they occupy a relatively small volume of the particular device we studied. Finally, we consider that electrons will assume a Druyvesteyn distribution if $kT_1 \ll \lambda E$, where E represents the magnitude of the electric field [25]. If we assume $kT_1 \sim 100$ eV in the region $r > R_c$, use values of λ from Table III, and consider a Laplacian potential, then this condition is widely satisfied for the operational regimes considered here.

REFERENCES

[1] P. T. Farnsworth, "Electric discharge device for producing interactions between nuclei," U.S. Patent 3 258 402, Jun. 28, 1966.

[2] P. T. Farnsworth, "Method and apparatus for producing nuclear-fusion reactions," U.S. Patent 3 386 883, Jun. 4, 1968.

[3] O. A. Lavrent'ev, "Electrostatic and electromagnetic high-temperature plasma traps," *Ann. N.Y. Acad. Sci.*, vol. 251, pp. 152–178, May 1975.

[4] B. Jurczyk, "Theory and development of a sealed deuterium–tritium inertial electrostatic confinement neutron generator," M.S. thesis, Univ. Illinois Urbana-Champaign, Champaign, IL, 1997.

[5] J. H. Nadler, "Space-charge dynamics and neutron generation in an inertial-electrostatic confinement device," Ph.D. dissertation, Univ. Illinois-Urbana-Champaign, Champaign, IL, 1992.

[6] J. H. Nadler, G. H. Miley, Y. Gu, and T. Hochberg, "Characterization of an Inertial Electrostatic Confinement Glow Discharge (IECGD) neutron generator," *Fus. Technol.*, vol. 21, pp. 1639–1643, May 1992.

[7] T. A. Hochberg, "Characterization and modelling of the gas discharge in a SFID neutron generator," M.S. thesis, Univ. Illinois-Urbana-Champaign, Champaign, IL, 1992.

[8] J. B. Javedani, Y. B. Gu, M. J. Williams, J. Hartwell, R. L. Anderl, G. H. Miley, J. H. Nadler, J. L. Jones, R. A. Nebel, and D. C. Barnes, "Studies of the IEC accelerator-plasma target fusion neutron source for activation analysis," *Bull. Amer. Phys. Soc.*, vol. 39, no. 7, p. 1768, 1994.

[9] G. H. Miley, J. DeMora, R. A. Anderl, J. H. Nadler, and R. Nebel, "Optimization of IEC grid design for maximum neutron production," *Fus. Technol.*, vol. 30, pp. 1315–1319, Dec. 1996.

[10] A. J. Satsangi, "Light intensity measurements of an inertial electrostatic confinement fusion plasma," M.S. thesis, Univ. Illinois-Urbana-Champaign, Champaign, IL, 1996.

[11] G. H. Miley, Y. Gu, J. M. Demora, R. A. Stubbers, T. A. Hochberg, J. H. Nadler, and R. A. Anderl, "Discharge characteristics of the spherical inertial electrostatic confinement (IEC) device," *IEEE Trans. Plasma Sci.*, vol. 25, no. 4, pp. 733–739, Aug. 1997.

[12] B. P. Bromley, "Approximate modeling of the inertial electrostatic confinement cylindrical device," M.S. thesis, Univ. Illinois-Urbana-Champaign, Champaign, IL, 1998.

[13] J. M. Demora, "Cathode grid optimization studies for the spherical inertial electrostatic confinement device," M.S. thesis, Univ. Illinois-Urbana-Champaign, Champaign, IL, 1999.

[14] Y. Gu and G. H. Miley, "Experimental study of potential structure in a spherical IEC fusion device," *IEEE Trans. Plasma Sci.*, vol. 28, no. 1, pp. 331–346, Feb. 2000.

[15] B. E. Jurczyk, "Research on edge ionization and star mode discharge physics in inertial electrostatic confinement neutron/proton sources," Ph.D. dissertation, Univ. Illinois-Urbana-Champaign, Champaign, IL, 2001.

[16] R. A. Stubbers, "Two dimensional modeling of a radially-convergent cylindrical Inertial Electrostatic Confinement (IEC) fusion device," Ph.D. dissertation, Univ. Illinois-Urbana-Champaign, Champaign, IL, 2002.

[17] R. L. Hirsch, "Inertial-electrostatic confinement of ionized fusion gases," *J. Appl. Phys.*, vol. 38, no. 11, p. 4522, Oct. 1967.

[18] C. C. Dobson and I. Hrbub, "Electron density and two-channel neutron emission measurements in steady-state spherical inertial–electrostatically confined plasmas, with review of the one-dimensional kinetic model," *J. Appl. Phys.*, vol. 96, no. 1, p. 94, Jul. 2004.

[19] I. H. Hutchinson, *Principles of Plasma Diagnostics*. Cambridge, U.K.: Cambridge Univ. Press, 2002, pp. 55–65.

[20] J. D. Swift and M. J. R. Schwar, *Electrical Probes for Plasma Diagnostics*. New York: American Elsevier, 1969.

[21] B. Chapman, *Glow Discharge Processes: Sputtering and Plasma Etching*. New York: Wiley-Interscience, 1980, p. 79.

[22] R. M. Meyer, Z. M. Smith, M. A. Prelas, and S. K. Loyalka, "Ion flow convergence in spherical inertial electrostatic confinement devices," *Phys. Plasmas*, vol. 15, no. 2, pp. 022 105-1–022 105-13, Feb. 2008.

[23] N. Hershkowitz, *Plasma Diagnostics*, O. Auciello and D. L. Flamm, Eds. New York: Academic, 1989.

[24] V. I. Demidov, S. V. Ratynskaia, and K. Rypdal, "Electric probes for plasmas: The link between theory and instrument," *Phys. Plasmas*, vol. 73, no. 10, p. 3409, Oct. 2002.

[25] M. J. Druyvesteyn and F. M. Penning, "The mechanism of electrical discharges in gases of low pressure," *Rev. Mod. Phys.*, vol. 12, no. 2, p. 87, Apr. 1940.

Ryan M. Meyer (M'00) received the B.S. degree in electrical engineering and the M.S. and Ph.D. degrees in nuclear engineering from the University of Missouri, Columbia, in 2002, 2004, and 2007, respectively.

He is currently a Lecturer with the Department of Electrical Engineering, Faculty of Engineering, Prince of Songkla University, Hat Yai, Thailand. His research has been focused on the theoretical and experimental studies of IEC devices.

Mark A. Prelas (M'80) received the Ph.D. degree from the University of Illinois at Urbana–Champaign, Urbana, in 1979.

In 1987, he was with the Idaho National Engineering Laboratory, U.S. Department of Energy. From 1999 to 2000, he was with the Bureau of Arms Control, U.S. Department of State. He is currently an H. O. Croft Professor of nuclear engineering with the University of Missouri-Columbia, Columbia. He has worked in the areas of arms control for weapons of mass destruction, the strategic defense initiative, the development of nuclear, chemical, and biological sensors, the synthesis and applications of wide-bandgap materials, directed-energy weapons, direct energy conversion, and gaseous electronics. He has published over 200 papers and 5 books. He is the holder of 12 national and international patents.

Dr. Prelas was the recipient of the Presidential Young Investigator Award in 1984. He was a Gas Research Institute Fellow in 1981, was a Fulbright Fellow at the University of New South Wales in 1992, was named a Fellow of the American Nuclear Society in 1999, and was a William C. Foster Fellow with the U.S. Department of State from 1999 to 2000.

Sudarshan K. Loyalka received the B.S. degree from the University of Rajasthan, Rajasthan, India, in 1964 and the M.S. and Ph.D. degrees from Stanford University, Stanford, CA, in 1965 and 1967, respectively.

He is currently a Curators' Professor of nuclear engineering and chemical engineering with the University of Missouri-Columbia, Columbia, where he has been the Director of their Particulate Systems Research Center since its inception in 1985. He has coauthored three books. His research and teaching interests include the areas of aerosol mechanics, rarefied-gas dynamics, and nuclear-reactor physics and safety.

Dr. Loyalka was elected as a Fellow of the American Institute of Physics for his contributions to understandings of the role of gas–surface interactions on transport processes in 1982. He was also elected as a Fellow of the American Nuclear Society for his contributions to aerosol mechanics, transport theory, nuclear-reactor physics and safety, and education of nuclear engineers in 1985. He was the recipient of the David Sinclair Award of the American Association of Aerosol Research for his sustained outstanding research in aerosol science and technology and the Glenn Murphy Award of the American Society for Engineering Education for education of nuclear engineers in 1995 and 1998, respectively.